PHYSICAL REVIEW B **96**, 035432 (2017)

Spin-resolved band structure of a densely packed Pb monolayer on Si(111)

C. Brand,[1] S. Muff,[2,3] M. Fanciulli,[2,3] H. Pfnür,[1,4] M. C. Tringides,[5,6] J. H. Dil,[2,3] and C. Tegenkamp[1,4,*]
[1]*Institut für Festkörperphysik, Leibniz Universität Hannover, Appelstraße 2, 30167 Hannover, Germany*
[2]*Swiss Light Source, Paul Scherrer Institut, 5232 Villigen PSI, Switzerland*
[3]*Institute of Physics, École Polytechnique Fédérale de Lausanne, 1015 Lausanne, Switzerland*
[4]*Laboratory of Nano and Quantum Engineering (LNQE), Leibniz Universität Hannover,*
Schneiderberg 39, 30167 Hannover, Germany
[5]*Ames Laboratory, U. S. Department of Energy, Iowa State University, Ames, Iowa 50011, USA*
[6]*Department of Physics and Astronomy, Iowa State University, Ames, Iowa 50011, USA*
(Received 12 May 2017; revised manuscript received 28 June 2017; published 24 July 2017)

Monolayer structures of Pb on Si(111) attracted recently considerable interest as superconductivity was found in these truly two-dimensional (2D) structures. In this study, we analyzed the electronic surface band structure of the so-called striped incommensurate Pb phase with $\frac{4}{3}$ ML coverage by means of spin-resolved photoemission spectroscopy. Our results fully agree with density functional theory calculations done by Ren *et al.* [Phys. Rev. B **94**, 075436 (2016)]. We observe a local Zeeman-type splitting of a fully occupied and spin-polarized surface band at the $\overline{\mathrm{K}}_{\sqrt{3}}$ points. The growth of this densely packed Pb structure results in the formation of imbalanced rotational domains, which triggered the detection of C_{3v} symmetry forbidden spin components for surface states around the Fermi energy. Moreover, the Fermi surface of the metallic surface state of this phase is Rashba spin split and revealed a pronounced warping. However, the 2D nesting vectors are incommensurate with the atomic structure, thus keeping this system rather immune against charge density wave formation and possibly enabling a superconducting behavior.

DOI: 10.1103/PhysRevB.96.035432

I. INTRODUCTION

Atomically thin two-dimensional (2D) overlayers of metals on semiconducting surfaces were shown to provide a powerful playground to study electronic correlation effects with utmost control of the atomic structure. Among others, charge density waves (CDW) [e.g., α-Pb/Ge(111)-($\sqrt{3}\times\sqrt{3}$) [1,2]] or Mott phases [α-Sn/Si(111)-($\sqrt{3}\times\sqrt{3}$) [3]], driven by strong electron-phonon and electron-electron interactions, were discovered for various (sub)monolayer phases. While many of these surface reconstructions come along with metal-insulator transitions, dense monolayers (MLs) of Pb and In on Si(111) reveal superconductivity with critical temperatures below 4 K [4–8].

Meanwhile, Pb/Si(111) became a prototypical system for studying multiple questions in nanoscience and surface science. The immiscibility of these elements provides an atomically sharp interface, which is a beneficial ingredient to understand the richness of the 2D phase diagram, the long-range ordering phenomena, and size effects. In this context, the Devil's staircase (DS) and striped incommensurate (SIC) phases as well as the quantum confinement-controlled film growth are often mentioned examples [9,10]. Aside from its superconducting behavior, the system was found very recently to provide also a new type of collective diffusion [11]. Albeit atomic details about the structure are intensively studied, less attention was paid to the electronic band structure. Moreover, the interpretation of former angle-resolved photoemission spectroscopy (ARPES) band structure measurements disagree with recent calculations [4,12,13].

Since many of these adlayers exhibiting the mentioned phenomena are built from heavy-Z elements, spin-orbit coupling becomes important, as illustrated by a controllable Rashba-type spin splitting [14,15], and reveals new exotic quantum phenomena, e.g., magnetically ordered phases in frustrated 2D systems [16] or strongly correlated spin-orbit entangled states, as recently shown for the quasi-1D DS phase of 1.31 ML Pb/Si(557) [17] by spin- and angle-resolved photoemission spectroscopy (SARPES) [18].

Within the isotropic Rashba-Bychkov (RB) model, the inversion asymmetry of the surface results in a shift of the surface bands in k space and formation of in-plane spin polarization with a vortical texture. The splitting occurs around time-reversal-invariant momenta (TRIMs), i.e., the $\overline{\Gamma}$ and $\overline{\mathrm{M}}$ points for the honeycomb lattice with C_{3v} symmetry, and is described by the Rashba Hamiltonian $H_{\mathrm{R}}(\mathbf{k}) = \alpha_{\mathrm{R}}(k_x\sigma_y - k_y\sigma_x)$, where $\sigma_{x,y}$ and $k_{x,y}$ denote the Pauli matrices and the in-plane wave-vector components, respectively [19,20]. The Rashba parameter α_{R} depends on details of the potential gradients and the wave functions [21]. Also, around non-TRIMs, the RB-type spin splitting can be described using the same model as it was shown for β-Bi/Si(111)-($\sqrt{3}\times\sqrt{3}$) [22]. The conventional surface band splitting with in-plane spin polarization was also observed around the $\overline{\mathrm{K}}$ points of the ($\sqrt{3}\times\sqrt{3}$) reconstruction (in the following referred to as $\overline{\mathrm{K}}_{\sqrt{3}}$; and similarly we use of $\overline{\Gamma}_{\sqrt{3}}$ and $\overline{\mathrm{M}}_{\sqrt{3}}$), which is the result of the local C_{3v} symmetry.

In systems where the effective masses of the charge carriers are wave-vector dependent, so-called unconventional RB effects are reported. For example, for the Au/Ge(111)-($\sqrt{3}\times\sqrt{3}$) system, at least third- and fifth-order corrections in k are mandatory to explain the z components of the spin-polarization vectors of the Fermi surface (FS) [23]. Moreover, a local Zeeman-type splitting with fully spin-polarized states along the surface normal was found recently at the $\overline{\mathrm{K}}$ point of the surface Brillouin zone (SBZ) of the (1×1) reconstruction

---

[*] tegenkamp@fkp.uni-hannover.de

for 1 ML Tl on Si(111) and Ge(111) [24,25]. The origin was explained as a result of the local C_3 symmetry around the $\overline{\mathrm{K}}$ points in systems of space group $p3m1$ giving rise to an effective magnetic field along the surface normal ($H_{\mathrm{SOC}} \propto \sigma_z B_z$) [26,27] in contrast to the typical RB in-plane effective B field. A possible combination of RB- and Zeeman-type spin splitting in a 2D system has also been discussed in theory [28].

The band structure of systems with strong correlation effects can further be distorted by spin-independent warping, which is related closely to effective Fermi nesting and incommensurate CDW formation [29,30]. Aside from the surface states of topological insulators [e.g., $Bi_2Te_3(111)$ [29], $Bi_2Se_3(111)$ [30]] and the Au/Ge(111)-($\sqrt{3}\times\sqrt{3}$) system [23,31], also β-Pb/Ge(111)-($\sqrt{3}\times\sqrt{3}$) [32] and the (2,6)-DS phase of Pb/Si(111) [33] show signatures of warping. Depending on the system's symmetry corrections of third or sixth order in k are considered for threefold and sixfold surfaces giving rise to a hexagonal shape of the FS.

In this study we concentrate on the most stable 2D phase of Pb/Si(111), i.e., the so-called SIC phase, which comprises the ideal $\frac{4}{3}$ ML coverage [34]. We present (S)ARPES measurements along various high-symmetry directions, in particular spin-integrated and spin-resolved momentum distribution curves (MDCs), as well as band maps. The SIC phase of Pb reveals locally a ($\sqrt{3}\times\sqrt{3}$) symmetry, but also supports the formation of domain walls (superstructures) and rotational domains. Both the symmetry as well as the imbalance between different rotational domains are considered in order to explain quantitatively the spin texture of the surface bands in k space.

II. EXPERIMENTAL SETUP

Si(111) samples (n-type doped) were cleaned *in situ* by degasing and subsequent flash annealing to 1150 °C until low-energy electron diffraction (LEED) revealed a brilliant (7×7) reconstruction. Pb was evaporated from a Knudsen cell and the amount was controlled by a quartz microbalance. The coverage was calibrated by various DS phases probed by Spot-Profile-Analysis-LEED [9] (SPA-LEED; $1\ \mathrm{ML} = 7.83\times10^{14}$ atoms per cm^2). Moreover, scanning tunneling microscopy (STM) is used for further information on the atomic structure. The STM experiments were performed in Hannover at room temperature and in Ames at low temperature.

SARPES measurements were conducted at the COPHEE end station at the SIS beamline of the Swiss Light Source [35]. The photoemission experiments were carried out with p-polarized light with a photon energy of $h\nu = 24$ eV at a base pressure of 1×10^{-10} mbar. By recording intensities and spin-induced scattering asymmetries with the two orthogonal Mott detectors for different emission angles, spin-resolved MDCs close to the Fermi energy were measured. In order to reveal acceptable signal-to-noise ratios, the spin-integrated and spin-resolved MDCs were taken 95 and 145 meV below E_{F}, respectively. All ARPES measurements were performed at low temperatures ($T = 75$–95 K). Details about the analysis of the spin data are outlined elsewhere, e.g., in Ref. [18].

III. EXPERIMENTAL RESULTS

A. Atomic structure of the SIC phase

A representative large-scale STM image and a high-resolution SPA-LEED pattern of the SIC phase are shown in Figs. 1(a) and 1(b), respectively. The structure of the ($\sqrt{3}\times\sqrt{3}$) reconstruction is schematically depicted in Fig. 1(f) within the green-shaded areas with the so-called H3 and T4 adsorption geometries. High-resolution STM images of both geometries are shown in Figs. 1(c) and 1(d), consistent with density functional theory (DFT) calculations [12,36]. These geometries, where the central Pb atom (orange colored) is either located above the hollow site of the Si honeycomb of the topmost Si bilayer or on top of the Si atom of the second Si layer, are energetically almost identical [37]. Hence, in densely packed Pb monolayer structures both positions are almost equally occupied in agreement with a recent high-resolution Raman study [38]. Both local geometries belong to $p31m$ space group, which is the same as for β-Bi/Si(111)-($\sqrt{3}\times\sqrt{3}$) [22].

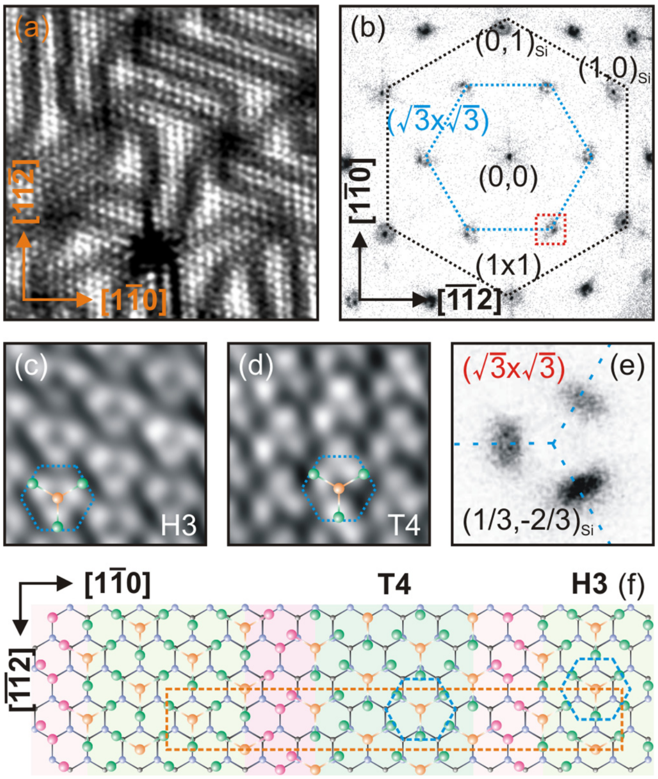

FIG. 1. Structure of the SIC phase of Pb/Si(111) comprising a coverage close to $\frac{4}{3}$ MLs of Pb. (a) Large-scale STM image (20 nm×20 nm, +1.5 V, 1 nA, 200 K, Ref. [37]). (b) SPA-LEED pattern with $E = 80$ eV. (c), (d) High-resolution STM images of the H3 and T4 geometry (2 nm×2 nm, +100 mV, 0.6 pA, 300 K), respectively. (e) A zoom into the SPA-LEED pattern shows a splitting of the ($\sqrt{3}\times\sqrt{3}$) reconstruction spots [cf. red rectangle in (b)]. (f) Top-view schematic for a domain-wall structure (superstructure) with ($\sqrt{3}\times\sqrt{3}$) reconstructions in H3 and T4 geometries separated by quasi-($\sqrt{7}\times\sqrt{3}$)-domain walls [($13\times\sqrt{3}$) superstructure with 1.308 ML coverage marked by the orange rectangle]. The unit cells for the local ($\sqrt{3}\times\sqrt{3}$) reconstruction in real and reciprocal space are indicated by blue-dashed hexagons.

The $(\sqrt{3}\times\sqrt{3})$ reconstruction contains ideally $\frac{4}{3}$ MLs of Pb and its periodic structure is nicely seen in SPA-LEED [Fig. 1(b)]. Moreover, the $(\sqrt{3}\times\sqrt{3})$ spots reveal a threefold splitting [enlarged in Fig. 1(e)] that is due to the formation superstructures with appearance of both H3 and T4 centered local reconstructions, which are separated by quasi-$(\sqrt{7}\times\sqrt{3})$-domain walls [39,40] as also visible in STM [Fig. 1(a); the $(13\times\sqrt{3})$ superstructure with 1.308 ML coverage is shown in Fig. 1(f) as an example] and rotational domains due to the symmetry of the Si(111) substrate. In addition, the superstructure formation is also related to the 5% mismatch of the bulk Pb- and Si(111)-lattice constants and the finite compressibility of the Pb atoms into $(\sqrt{3}\times\sqrt{3})$ positions [39]. Most importantly, the formation of superstructures and domains comes along with breaking of the local C_{3v} symmetry of the $(\sqrt{3}\times\sqrt{3})$ reconstruction. We will show that the resulting C_1 symmetry in presence of an imbalanced distribution of the SIC rotational domains explains the finite spin-polarization components S_x and S_z along the $\overline{\Gamma \mathrm{M}}$ direction (k_x direction).

B. Constant energy map of the SIC phase

The constant energy map (CEM) shown in Fig. 2(a) was taken 178 meV below E_{F}. For a better orientation, the boundaries for SBZs and symmetry points of Si(111)-(1×1) and the $(\sqrt{3}\times\sqrt{3})$ reconstruction are superimposed. The entire Brillouin zone is schematically depicted in Fig. 2(b). It is obvious that the CEM deviates strongly from the energy isosurface of an almost free electron gas. It shows electronlike hexagonally shaped and holelike boomerang-shaped pockets with threefold rotational symmetry around the $\overline{\Gamma}_{\sqrt{3}}$ and $\overline{\mathrm{K}}_{\sqrt{3}}$ points, respectively. The appearance of the hexagonally shaped state is in good agreement with the FS obtained in a recent density functional theory (DFT) calculation [13]. The CEM reflects mainly the $(\sqrt{3}\times\sqrt{3})$ periodicity, because ARPES is rather insensitive to the long-range order of the SIC phase. In particular, the flattening of the isoenergy lines seen in Fig. 2(a) turns out to be a characteristic signature and, e.g., is important for an effective Fermi nesting in similar 2D systems [1,41]. Except for the holelike pockets around the $\overline{\mathrm{K}}_{\sqrt{3}}$ points an almost identical FS was found for β-Pb/Ge(111)-$(\sqrt{3}\times\sqrt{3})$ [32]. In contrast, both states are found in the similar (2,6)-DS phase of Pb/Si(111) with 1.286 ML coverage [with $(14\times\sqrt{3})$ supercell] except for the additional splitting of the hexagons due to the ×14 periodicity [33]. Similar to related systems, the photoelectron intensity within the first SBZ of the $(\sqrt{3}\times\sqrt{3})$ reconstruction is strongly reduced due to a matrix element effect [23,42]. In the following, we will first discuss the surface bands and their spin character. These findings will be correlated with recent DFT calculations [12,13].

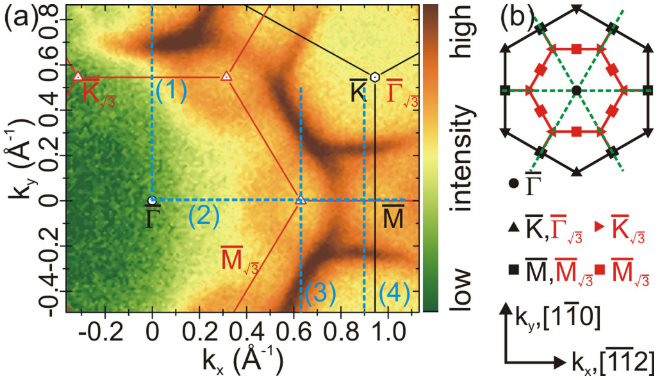

FIG. 2. (a) CEM of the SIC phase taken 178 meV below E_{F}. The black and red lines represent the borders of the first SBZs of the Si(111) and $(\sqrt{3}\times\sqrt{3})$ reconstruction, respectively. The blue dashed lines (1–4) denote directions at which MDCs and band maps were taken. (b) Schematic of the SBZs for the Si(111)-(1×1) substrate (black) and the $(\sqrt{3}\times\sqrt{3})$ reconstruction (red). The k_x and k_y directions are along the $[\bar{1}\bar{1}2]$ and $[1\bar{1}0]$ directions, respectively. The dashed green lines denote the mirror planes of the $(\sqrt{3}\times\sqrt{3})$ reconstruction in reciprocal space.

C. Band maps and momentum distribution curves

Details of the band structure taken along the $\overline{\Gamma \mathrm{K}}$ direction are shown in Fig. 3. Clearly, a metallic surface band, denoted by S1, crosses the Fermi energy at $k_y \approx 0.7$ Å^{-1}. Further details become obvious when looking at the d^2I/dE^2 map shown in Fig. 3(c). Negative values of d^2I/dE^2 are indicative for the appearance of a band. The Si-valence band maximum (VBM) is located around 170 meV below E_{F}. As we will show in context of the spin-resolved ARPES data, all surface bands are spin split. However, the Rashba splitting $\Delta k_y \approx 0.04$ Å^{-1} of the SIC phase is comparably small, thus the surface bands appear rather broad and diffuse. The spin-split states are indicated by dashed lines in Fig. 3(c). The presence of a doublet structure within the S1 state is also mandatory when fitting the spin-integrated MDC taken 95 meV below E_{F} and shown in Fig. 3(a). The MDC comprises very faintly also the S1 state within the first SBZ of the $(\sqrt{3}\times\sqrt{3})$ reconstruction, symmetrically with respect to the $\overline{\mathrm{M}}_{\sqrt{3}}$ point. Its strong reduction in intensity is again most likely due to the matrix element effect like seen for the CEM in Fig. 2(a) [42]. Within the model of a nearly free-electron gas the effective mass of the S1 state along the k_y direction is approximately $0.42\,m_{\mathrm{e}}$ near E_{F}, where m_{e} denotes the free-electron mass. Indeed, we will show in the context of warping effects that this model is not appropriate for the SIC phase. A second surface state, labeled as S2 in Fig. 3(c), is located around 650 meV below E_{F}.

A similar analysis was performed along the $\overline{\Gamma \mathrm{M}}$ direction and is shown in Fig. 4. The band map reveals again the S1-surface state, which crosses E_{F} at $k_x \approx 0.4$ Å^{-1} and forms additionally a small electron pocket around E_{F} at $k_x \approx 0.75$ Å^{-1} in full agreement with recent DFT calculations [12,13]. Compared to the DFT calculations, the chemical potential in our experiment is shifted by around 130 meV, thus, the S1 state crosses E_{F} three times between the $\overline{\Gamma}$ and the $\overline{\mathrm{M}}$ points. A similar value of the chemical potential was measured previously [4]. The Rashba splitting $\Delta k_x = 0.04$ Å^{-1} of S1 in the $\overline{\Gamma \mathrm{K}}_{\sqrt{3}}$ range is the same as in the $\overline{\Gamma \mathrm{K}}$ direction. The effective mass of the S1 band, starting from the $\overline{\Gamma}$ point, is $0.77\,m_{\mathrm{e}}$ near E_{F}, i.e., the bands along the $\overline{\Gamma \mathrm{K}}$ direction reveal a significantly lower value (around 45%) indicating

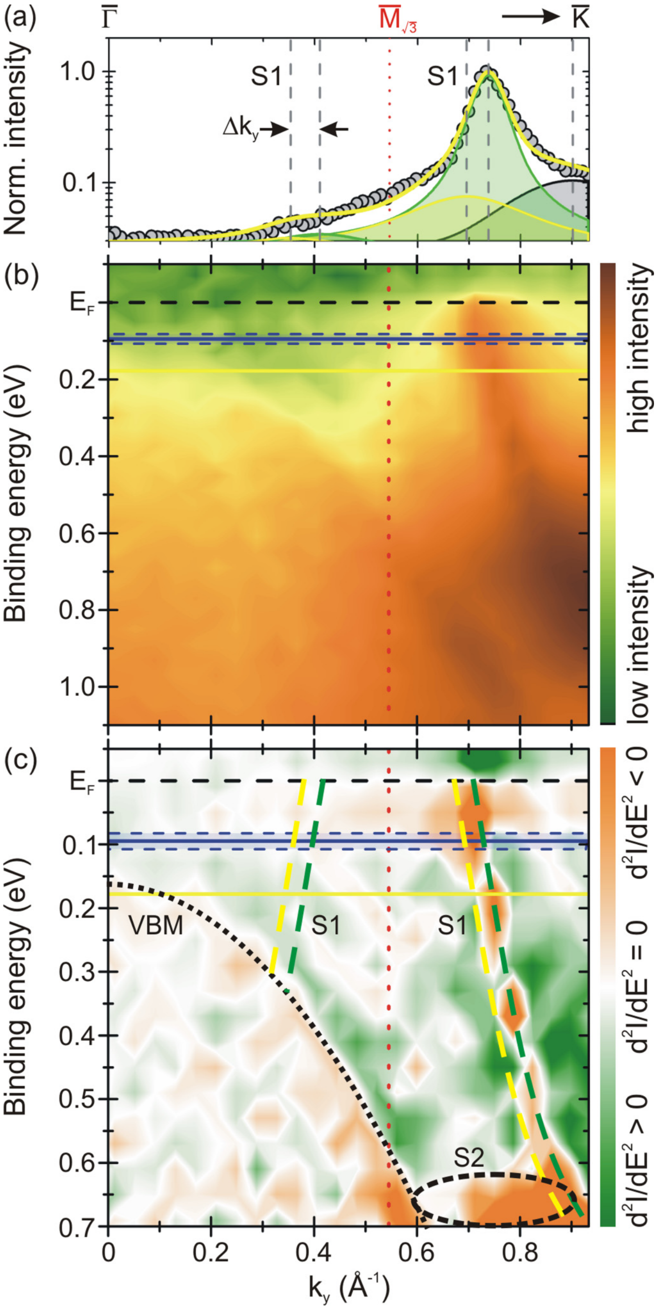

FIG. 3. Band structure of the SIC phase along the $\overline{\Gamma K}$ direction [direction (1) in Fig. 2(a)]. The red dotted line denotes the position of the $\overline{M}_{\sqrt{3}}$ point. (a) Spin-integrated MDC taken at $E = 95$ meV [see bluish area in panels (b) and (c)]. (b) The band map shows clearly the metallic surface band S1 crossing E_F at $k_y \approx 0.7$ Å^{-1}in the second SBZ of the $(\sqrt{3}\times\sqrt{3})$ reconstruction. (c) Map of the second derivative of the intensity towards energy d^2I/dE^2 to highlight details of the band structure. Also, the S1 band in the first SBZ of the $(\sqrt{3}\times\sqrt{3})$ reconstruction is shown. The yellow and green dashed lines indicate the Rashba splitting Δk_y of the S1 state. The horizontal yellow and blue lines show the energy, where the CEM and MDC have been taken, respectively. Only indications of the S2 band are visible. VBM denotes the Si-valence band maximum.

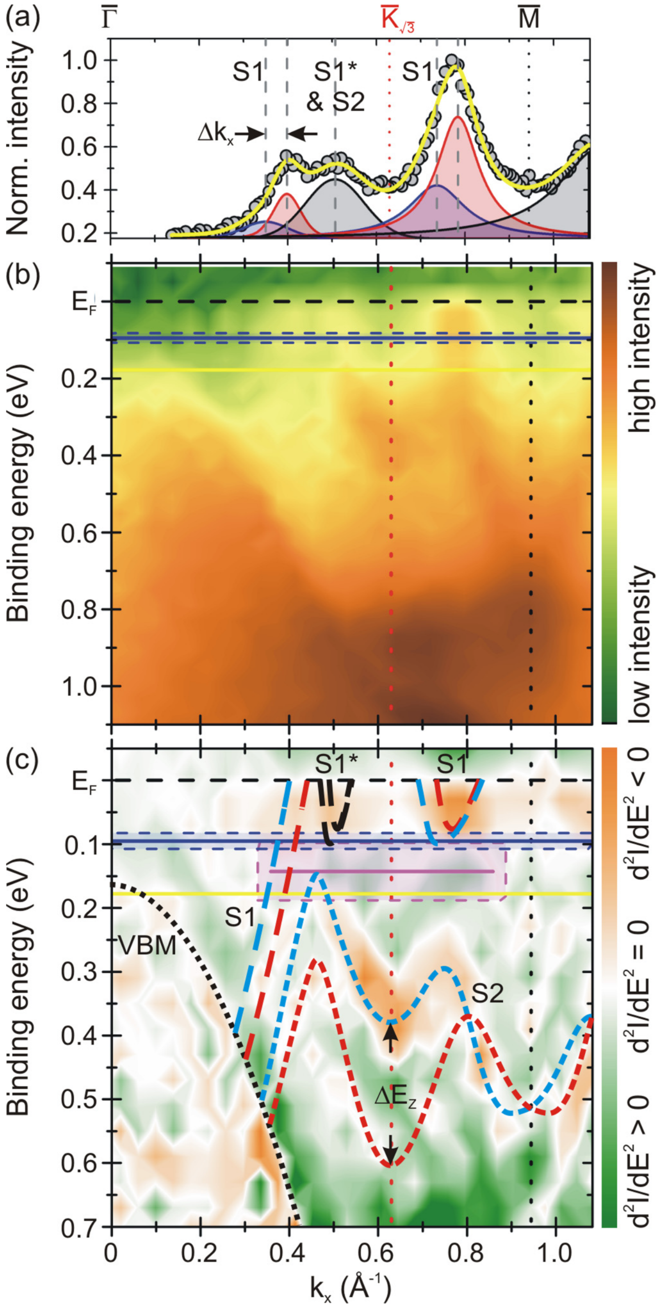

FIG. 4. Band structure of the SIC phase along the $\overline{\Gamma M}$ direction [direction (2) in Fig. 2(a)]. The red (black) dotted line denotes the position of the $\overline{K}_{\sqrt{3}}$ point ($\overline{M}$ point). (a) Spin-integrated MDC taken at $E = 95$ meV [see bluish area in (b) and (c)]. (b) The band map shows the metallic surface band S1 and the fully occupied surface band S2. (c) d^2I/dE^2 map of (b) to highlight details of the band structure. The magenta-shaded box denotes the phase space where spin-resolved measurements (shown in Fig. 6) have been taken, and the horizontal yellow line indicates the cut of the CEM in Fig. 2(a). The progression of the S2 state is taken from Ref. [13] and is in good agreement with the experiment. The Rashba splitting of S1 is $\Delta k_x = 0.04$ Å^{-1}. S1* denotes the projection of the S1 states originating from the other two equivalent $\overline{K}_{\sqrt{3}}\overline{M}_{\sqrt{3}}$ directions.

the strong directional band renormalization as it is obvious already from the CEM in Fig. 2(a). Inspection of Fig. 4(c) and the corresponding spin-integrated MDC in Fig. 4(a) reveals further an intensity feature denoted by S1* close to E_F at $k_x = 0.5$ Å^{-1}, which is located symmetrically to the S1 state at $k_x \approx 0.75$ Å^{-1}with respect to the $\overline{K}_{\sqrt{3}}$ point. Due to the threefold rotational symmetry of the ($\sqrt{3}\times\sqrt{3}$) reconstruction, the S1* feature is induced by the projection of the (reentered) S1 state of the equivalent $\overline{\mathrm{K}}_{\sqrt{3}}\overline{\mathrm{M}}_{\sqrt{3}}$ directions [12,13].

Most remarkably, the intensity feature located at the $\overline{\mathrm{K}}_{\sqrt{3}}$ point with a binding energy of 0.4 eV is not the minimum of a surface band that crosses E_F, but belongs to the second spin-split surface band S2 that is fully occupied. This finding is in contrast to a previous interpretation [4]. As it becomes obvious from the d^2I/dE^2 map of the band map shown in Fig. 4(c), this band reveals clearly a gap towards the Fermi energy since $d^2I/dE^2 > 0$. The S2 state is highlighted with the dispersions extracted from the DFT calculation done by Ren *et al.* (Ref. [13]). The local Zeeman-type splitting ΔE_Z at the $\overline{\mathrm{K}}_{\sqrt{3}}$ point of the H3 geometry was calculated to be 300 meV, while for the T4 structure ΔE_Z is lowered to 136 meV [13]. In both cases, the spin-polarized bands of S2 cross each other at $k_x \approx 0.8$ Å^{-1} and are again degenerate at the $\overline{\mathrm{M}}$ and $\overline{\mathrm{M}}_{\sqrt{3}}$ points, thus showing a Rashba splitting. The strong influence of the adsorption geometry on ΔE_Z nicely reflects the sensitivity of the spin-orbit interaction on details of the atomic environment, although the formation energies for both configurations are almost identical [37]. Since the exact value of the local Zeeman-type splitting differs, the coexistence of both structures within the superstructure of the SIC phase triggers also a smearing of the photoelectron intensity, obviously visible around the $\overline{\mathrm{K}}_{\sqrt{3}}$ points of the S2 state seen in Figs. 4(b) and 4(c).

Finally, the band structure along the $\overline{\mathrm{KMK}}$ direction was measured (Fig. 5). Again, the S1 state crosses E_F as obvious from the band map in Fig. 5(b) at $k_y \approx 0.23$ Å^{-1}. The spin-integrated MDC in Fig. 5(a) shows that each of the intense S1 bands is accompanied by a satellite peak shifted by 0.04 Å^{-1}showing the size of the Rashba splitting Δk_y. The intensity located at 650 meV binding energy and low values of k_y can again be assigned to the S2-surface band also showing a Rashba splitting around the $\overline{\mathrm{M}}$ point, in agreement with DFT calculations [12,13]. From symmetry considerations it should be mentioned that this part of the S2 band is equivalent to the S2 state encircled in Fig. 3(c).

To summarize this section, the measured band structure of the SIC phase is in good agreement with DFT calculations. Partly, the limited resolution is accounted for by the small Rashba splitting in k space as well the different Zeeman-type splittings, expected for the H3 and T4 structures of the ($\sqrt{3}\times\sqrt{3}$) reconstruction within the SIC phase.

D. Spin-resolved ARPES measurements

Details on the spin polarizations of the surface bands were deduced from spin-resolved ARPES data taken 145 meV below E_F and are shown in Fig. 6. Although the amplitudes of the measured spin components are lower than 25% as visible in Figs. 6(b) and 6(d), the spin polarization of each band can be much higher since the overlap of the intensities from the bands reduces the overall spin polarization. Details regarding the spin polarizations obtained by the data analysis are summarized in Tables I and II and will be discussed in more detail below.

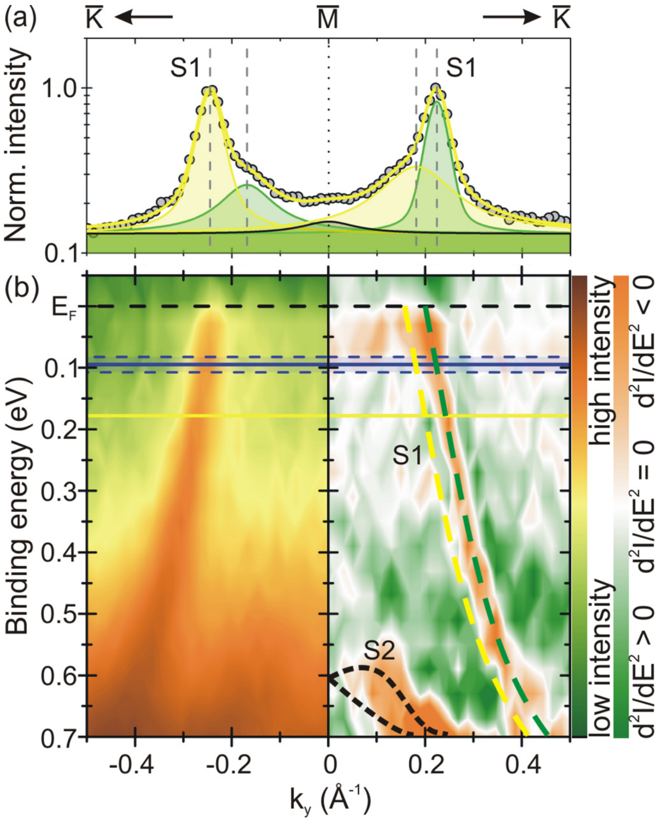

FIG. 5. Band structure of the SIC phase parallel to the $\overline{\mathrm{KMK}}$ direction at $k_x = 0.90$ Å^{-1}[cf. with line (4) in Fig. 2(a)]. (a) The MDC taken 95 meV below E_F [see bluish area in right part of (b)] clearly shows a splitting due to the Rashba effect. (b) The band map on the left part and the d^2I/dE^2 map on the right part show the metallic S1 state as well as the spin-split state S2 at higher binding energies. The horizontal yellow line indicates the cut of the CEM in Fig. 2(a).

In Figs. 6(a) and 6(b), the results of the k_y direction cutting through the $\overline{\mathrm{K}}_{\sqrt{3}}$ point at $k_x = 0.63$ Å^{-1} [direction (3) in Fig. 2(a)] are shown. The corresponding MDC [Fig. 6(a)] reveals three peaks on each side symmetrically with respect to $k_y = 0$ Å^{-1}. The outer two peaks on each side of the spectrum (labeled with **a**, **b**, **e**, and **f**) are assigned to the S1 state in the second SBZ of the ($\sqrt{3}\times\sqrt{3}$) reconstruction. Therefore, the spin vector is pairwise reversed for S_x and S_y, showing again the Rashba-type behavior of S1 in this part of the k space. The apparently larger splitting $\delta k_y \approx 0.1$ Å^{-1}of the peaks **a**, **b** and **e**, **f** compared to the $\overline{\Gamma\mathrm{K}}$ and $\overline{\Gamma\mathrm{M}}$ directions is due to the intersection under a finite angle (≈60°) with respect to the high-symmetry directions. Moreover, the S_z components at these k points are nonzero in consistency with the Rashba model including third-order terms within C_{3v} symmetry [43,44]. In other words, the existence of finite S_z components corroborates that higher-order Rashba terms are necessary for the description of the band structure. The interpretation of the two peaks in between the S1 states of the MDC in Fig. 6(a) (labeled with **c** and **d**) is not as straightforward because the energy window of the spin-resolved measurements crosses various states. Details of their spin components, in particular

TABLE I. Peak parameters of the spin-resolved MDC taken along the k_y direction through the $\overline{\mathrm{K}}_{\sqrt{3}}$ point at $k_x = 0.63$ Å^{-1}. The peaks denoted by **a–f** are labeled in Fig. 6(a). The spin components in the right part of the table are calculated by Eqs. (2) and (3) with the experimental values of S.

			Spin components					
	Position	Polarization	Experiment			C_{3v} Rashba model		
Band, peak	k_y (Å^{-1})	S (%)	S_x (%)	S_y (%)	S_z (%)	S_x (%)	S_y (%)	S_z (%)
S1, **a**	− 0.34	26.0	+6.1	+25.3	+0.9	+12.2	+18.9	(−13.1)
S1, **b**	− 0.23	49.1	− 27.8	− 15.4	+37.4	−31.5	−30.8	+21.7
S1*/S2, **c**	− 0.15	99.9	− 39.1	+9.8	− 91.4			
S1*/S2, **d**	0.16	56.1	+14.0	+12.7	+52.8			
S1, **e**	0.25	22.9	+15.6	− 6.5	− 15.5	+14.0	−14.7	−10.6
S1, **f**	0.36	27.6	− 14.6	+16.8	− 16.3	−12.2	+20.6	(+13.7)

the pronounced amplitudes and strong correlation of the S_x and S_z components, will be discussed below.

The results for the $\overline{\Gamma\mathrm{M}}$ direction (here k_x direction, with $k_y = 0$ Å^{-1}) are shown in Figs. 6(c) and 6(d). Again, the spin-resolved measurements were done 145 meV below E_F, i.e., the S1, S1*, and S2 bands marginally overlap with the energy window of the detector [the integration area is marked by the magenta-shaded area in Fig. 4(c)], such that the spin polarization of each band can be determined clearly. The interpretation of the spin texture along the $\overline{\Gamma\mathrm{M}}$ direction is more challenging, but an interpretation of the data is still possible since thermal broadening of the states results in finite intensities in the MDC. The Rashba-split S1 states are responsible for the intensity at $k_x \approx 0.4$ Å^{-1} [Fig. 6(c), peaks labeled by **a** and **b**]. The intensity of peak **c** at $k_x = 0.5$ Å^{-1} reveals a spin-down S_y polarization, which is mainly addressed to the upper S2 band [cf. Fig. 4(c)]. However, also the S1* state is within the energy window of the detector and its spin texture is superimposed onto the spin texture of the S2 state, but with less portion. Around $k_x = 0.75$ Å^{-1}, the second maximum in energy of the S2 band is out of the range of the energy window of the spin-resolved measurement and rather the spin texture of the S1 band is probed. The change of the spin direction around $k_x = 0.8$ Å^{-1} is caused by the reversed spin partner within the S1 pocket [peaks labeled by **d** and **e** in Fig. 6(c)].

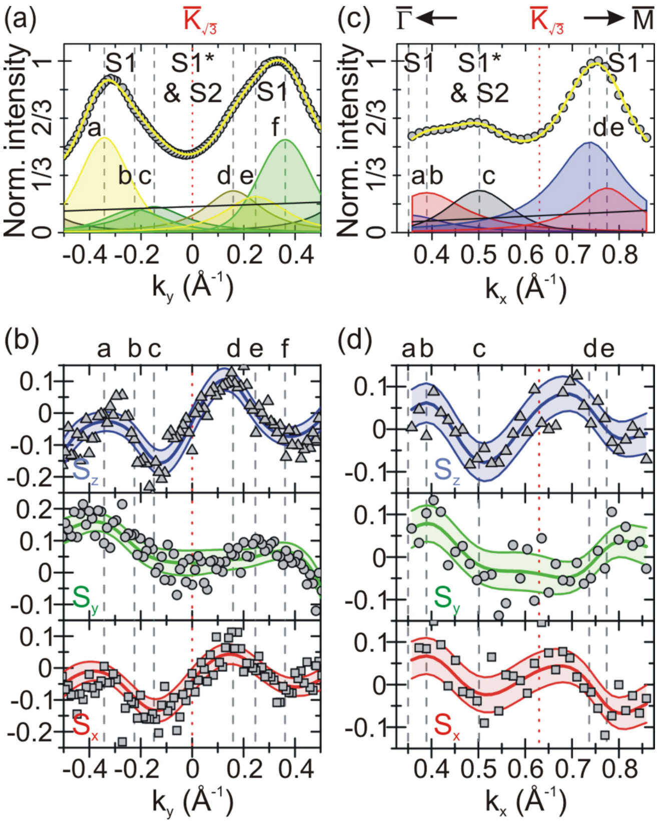

FIG. 6. Spin-resolved MDCs (a), (c) and corresponding spin-polarization vector components (b), (d) along the k_y direction through the $\overline{\mathrm{K}}_{\sqrt{3}}$ point [(a), (b), cf. direction (3) in Fig. 2(a)] and along the $\overline{\Gamma\mathrm{M}}$ direction [(c), (d), cf. direction (2) in Fig. 2(a)] taken 145 meV below E_F. The shaded areas in (b) and (d) account for the uncertainty of the simultaneous fitting of all four data sets, i.e., S_x, S_y, S_z and the MDC. Details of the fit parameters for the individual peaks (labeled by **a-f**) are summarized in Tables I and II.

IV. DISCUSSION

A. Characterization of the CEM

Based on these results, the CEM, introduced in context of Fig. 2(a), can be fully characterized. Figure 7 shows a schematic of the hexagonlike and pocketlike structures around the $\overline{\Gamma}_{\sqrt{3}}$ and $\overline{\mathrm{K}}_{\sqrt{3}}$ points, respectively. When ignoring symmetry breaking due to SIC superstructure and domain formation, the local TRS of the spin-polarized states is maintained with respect to the $\overline{\Gamma}_{\sqrt{3}}$ and $\overline{\mathrm{M}}_{\sqrt{3}}$ points, and is only broken directly at the $\overline{\mathrm{K}}_{\sqrt{3}}$ points. Moreover, the states around the $\overline{\Gamma}_{\sqrt{3}}$ and $\overline{\mathrm{K}}_{\sqrt{3}}$ points show C_{3v} symmetry, while around the $\overline{\mathrm{M}}_{\sqrt{3}}$ points there is C_{1h} symmetry.

In order to estimate the charge carriers for transport, only the S1 and S1* states are relevant for the following discussion. For the hexagonally shaped Fermi surface of the S1 state the

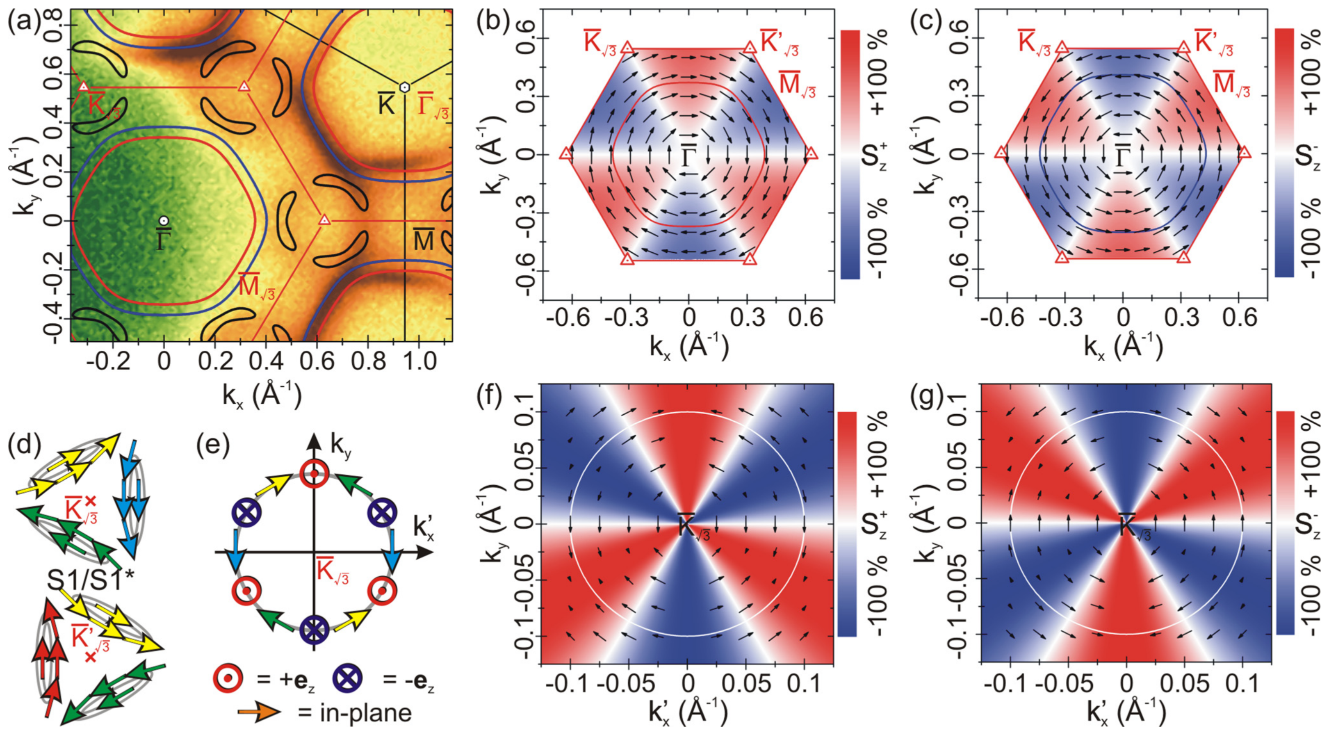

FIG. 7. Modeling of the band structure and spin texture. (a) CEM taken 178 meV below $E_{\rm F}$. The spin-polarized constant energy contours (red and blue lines) of the S1 states are deduced from nonlinear Rashba and warping terms. The threefold-symmetric boomerang-shaped isoenergy lines originate from the S2 state. (b), (c) Spin texture of the $S1^+$ and $S1^-$ states around the $\overline{\Gamma}$ point. The arrows indicate the orientation and strength of the in-plane components, while S_z is color coded. The hexagonally warped lines show the isoenergy lines at $E_{\rm F}$. Values at certain (k_x,k_y) points of the S1 state are reported in Tables I and II and are compared with the experiment. (d) In-plane spin texture around the $\overline{\rm K}_{\sqrt{3}}$ points of the S1/S1* state at $E_{\rm F}$ showing opposite spin polarization of the inner and outer ellipses, respectively. (e) Orientation of the effective magnetic field of the S2 state around the $\overline{\rm K}_{\sqrt{3}}$ point, which generates the spin textures shown in (f) and (g). (f), (g) Spin texture of the $S2^+$ and $S2^-$ states around the $\overline{\rm K}_{\sqrt{3}}$ point. The circles are isoenergy lines at 300 and 400 meV binding energy, respectively. The modeling of the spin texture has been done with a spin polarization of $S = 100\%$. The k_x values are given with respect to the $\overline{\rm K}_{\sqrt{3}}$ point.

electron density is given by $n_{\rm Hex} = 3\sqrt{3}[\bar{k}_{\rm F,x}/(2\pi)]^2$, where $\bar{k}_{\rm F,x} \approx 0.45$ Å^{-1} is the spin-averaged Fermi wave vector along the $\overline{\Gamma \rm M}$ direction, resulting in an electron density of $n_{\rm Hex} \approx 2.23\times10^{14}$ cm^{-2}. The carrier concentration of the ellipse-shaped pockets of the S1/S1* state within the first SBZ of the $(\sqrt{3}\times\sqrt{3})$ reconstruction near the $\overline{\rm K}_{\sqrt{3}}$ points is in total $n_{\rm S1/S1^*} \approx 5\times10^{13}$ cm^{-2}. The value of the total carrier concentration of $n \approx 2.73\times10^{14}$ cm^{-2} is in perfect agreement with the value deduced from the calculated band structure [12,13]. Compared to the Pb-adatom density of 1.04×10^{15} cm^{-2} ($\frac{4}{3}$ ML phase), every Pb atom within the $(\sqrt{3}\times\sqrt{3})$ unit cell donates $\frac{1}{4}$ electron into the metallic S1 state. Similarly to the Tl/Si(111) system [26] we assume that only the Pb$6p^2$ electrons are involved in the bonding formation. The $6s^2$ electrons are energetically 6 eV below the p orbitals and do not contribute to the band structure around the Fermi level, thus, eight p electrons per $(\sqrt{3}\times\sqrt{3})$ unit cell are participating in the bond formation. While three of these electrons form rather localized states with the three, the Si atoms of the topmost Si layer (overlap of Pb$6p_z$ with Si$3sp^3$), five electrons are left for the $(\sqrt{3}\times\sqrt{3})$ reconstruction, such that three surface bands are formed with $6p_xp_y$ character, of which one is only half-filled (S1) [45]. Aside from the fully occupied S2 band, there is a second fully occupied band, but at higher binding energies [12,13].

The Rashba splitting of the S1 state around $E_{\rm F}$ is comparable to what was measured for the β-Pb/Ge(111)-$(\sqrt{3}\times\sqrt{3})$ phase with the same Pb coverage, but lower Pb density due to the larger Ge-lattice constant compared with Si [32,45]. Also, for 1.31 ML Pb/Si(557) similar values for direction along the wires ($\overline{\Gamma \rm K}$ direction) were found, while the spin splitting in the $\overline{\Gamma \rm M}$ direction (across the wires) is about five times larger due to electronic correlation effects [17].

Apparently, the S1 (S1*) and S2 surface bands around the $\overline{\rm K}_{\sqrt{3}}$ points along the $\overline{\Gamma \rm M}$ direction reveal pronounced out-of-plane S_z components. In contrast to the $\overline{\Gamma \rm K}$ direction, the S_x and S_z components, measured along the $\overline{\Gamma \rm M}$ direction, should entirely vanish because of the mirror symmetry of the $(\sqrt{3}\times\sqrt{3})$ reconstruction. This argument still holds if higher orders of the Rashba expansion are considered. As mentioned, the presence of rotational C_{3v} symmetry gives rise to the threefold S1/S1* states around the $\overline{\rm K}_{\sqrt{3}}$ points, i.e., the S_x and S_z components of the S1* states need exactly to cancel out each other. This situation is depicted in Fig. 7(d) for the S_x components of the S1/S1* pocket around the $\overline{\rm K}_{\sqrt{3}}$ points. The same should hold if equally sized and distributed rotational domains are present, which show C_1 symmetry without any mirror symmetry, giving rise to Rashba terms containing $\sigma_{x,z}$ along the $\overline{\Gamma\mathrm{M}}$ direction [43]. Therefore, any finite value of the S_x and S_z components along this direction is directly related to an imbalance of these rotational domains with respect to their size and distribution. This imbalance of the rotational domains, as deduced from ARPES, is in agreement with the imbalance of the intensity seen in SPA-LEED across the superstructure-induced splitting of the $(\sqrt{3}\times\sqrt{3})$ spots [cf. Fig. 1(e)].

Near the $\overline{\mathrm{K}}_{\sqrt{3}}$ point, the effective Hamiltonian of the S2 state along the $\overline{\Gamma\mathrm{M}}$ direction (k_x direction) reads as $\mathrm{H}_x \propto B_y\sigma_y$, with an effective magnetic field B_y pointing in the y direction. Due to the mirror plane along the $\overline{\Gamma\mathrm{M}}$ direction, $B_x\sigma_x$ and $B_z\sigma_z$ terms are missing as otherwise the time-reversal symmetry (TRS) is violated. As already mentioned in the context of the discussion along the $\overline{\Gamma\mathrm{K}}$ direction, the existence of S_z components in all the other directions is allowed within C_{3v} symmetry, if higher-order Rashba- and/or internal Zeeman-type effects are considered [43]. Please note, in contrast to Tl/Ge(111) [25] and Tl/Si(111) [26], the shift in energy of the S2 surface band in $\overline{\Gamma\mathrm{M}}$ direction at the $\overline{\mathrm{K}}_{\sqrt{3}}$ point is due to an effective magnetic field in the y direction rather than in the z direction.

B. Modeling of the band structure and spin texture of the SIC phase

In the following, we will model the bands and spin textures of the S1 and S2 bands, thereby relying on C_{3v} symmetry for the sake of simplicity. The imbalance of rotational domains is not taken into account.

In the context of the spin components presented in the context of Fig. 6, we already pointed out that higher-order Rashba terms are mandatory in order to explain the out-of-plane spin components. Such corrections to the linear Rashba model are particularly important for half-filled bands, where curvature effects of the band structure severely feed back to the effective mass of the charge carriers close to the Fermi surface. Implicitly, the S1 state was treated so far in terms of a nearly free-electron-gas system. However, as shown by the DFT calculations done by Sakong *et al.* and Ren *et al.* (Refs. [12,13]), the S1 surface band is strongly altered due to hybridization with energetically low-lying Si states, thus giving rise to a strong $\mathbf{k}$ dependence of the effective mass along the entire SBZ. This anisotropy of the effective mass gives rise to warping effects, i.e., a deviation from circular isoenergy lines, like those seen in Fig. 2(a).

In this analysis we included these effects via a Hamiltonian with terms up to the order of k^6. In detail, we fitted the band structure of our experimental data for the S1 state around the $\overline{\Gamma}$ point by means of

$$E_\pm(\mathbf{k}) = E_0 + \frac{\hbar^2k^2}{2m_0^*} + \kappa k^4 + [\eta - \chi\cos(6\varphi)]k^6 \pm\sqrt{\left(\alpha_1^I k + \alpha_3^I k^3\right)^2 + \left(\alpha_3^A\right)^2 k^6 \sin^2(3\varphi)}\,, \tag{1}$$

where $E_0 = -663$ meV and $m_0^* = 3\,m_\mathrm{e}$ denote the energy and effective mass at the $\overline{\Gamma}$ point, $\alpha_1^\mathrm{I} = -170$ meV Å, $\alpha_3^\mathrm{I} = -835$ meV Å^3, $\alpha_3^\mathrm{A} = -1.209$ eV Å^3 are the first-/third-order isotropic/anisotropic Rashba parameters [43,44], $\kappa = 8.267$ eV Å^4 and $\eta = 60.008$ eV Å^6 are isotropic deviations from the nearly free-electron gas, while $\chi = 17.184$ eV Å^6 characterizes the size of the warping. The angle φ and k are defined by the Cartesian coordinates $k_x = k\cos\varphi$, $k_y = k\sin\varphi$. The first line of Eq. (1) describes the contribution of the spin-independent part, while the second line is related to the spin-dependent Rashba effect with terms up to the order of k^3. The lowest possible spin-independent anisotropy in C_{3v} symmetry is given by the χk^6 term.

As a consequence, the effective mass m^* of the S1 band at the Fermi energy is depending on the direction and the spin-polarized subband. The fitting of Eq. (1) to the experimental data yields $m^{*,+}_{\mathrm{F},x} = 0.152m_\mathrm{e}$, $m^{*,-}_{\mathrm{F},x} = 0.12m_\mathrm{e}$, $m^{*,+}_{\mathrm{F},y} = 0.119m_\mathrm{e}$ and $m^{*,-}_{\mathrm{F},y} = 0.094m_\mathrm{e}$, showing strongly reduced values with respect to the nearly free-electron gas. A calculation treating the dispersion as quasirelativistic gives similar values. The result of the dispersion fit is shown in Fig. 7(a) for the S1 state taken at 178 meV below E_F. Apparently, the modeling nicely reproduces the pronounced flattening.

Moreover, at this energy the isosurface intersects partly also the S2 state (cf. with yellow line in Fig. 4) giving rise to the boomerang-shaped structures around the $\overline{\mathrm{K}}_{\sqrt{3}}$ points, where apparently warping is only of minor importance.

Relying on the Rashba parameters, finally also the full spin vector $\mathbf{S}^\pm(\mathbf{k})$ can be calculated via

$$\mathbf{S}^\pm(\mathbf{k}) = \pm\frac{\hbar}{2}\cdot\frac{\boldsymbol{\alpha}(\mathbf{k})}{|\boldsymbol{\alpha}(\mathbf{k})|}\cdot S^\pm\,, \tag{2}$$

where $S^\pm$ is the gradual spin polarization of the state, and

$$\boldsymbol{\alpha}(\mathbf{k}) = \begin{pmatrix} -\sin\varphi\left(\alpha_1^\mathrm{I}k + \alpha_3^\mathrm{I}k^3\right) \\ \cos\varphi\left(\alpha_1^\mathrm{I}k + \alpha_3^\mathrm{I}k^3\right) \\ \sin(3\varphi)\,\alpha_3^\mathrm{A}k^3 \end{pmatrix} \tag{3}$$

is derived from writing the Rashba Hamiltonian as $H_\mathrm{R}(\mathbf{k}) = \boldsymbol{\alpha}(\mathbf{k})\cdot\boldsymbol{\sigma}$, $\boldsymbol{\sigma}$ being the vector of the Pauli matrices [43,44].

The resulting spin textures are shown in Fig. 7 for the S1 [Figs. 7(b) and 7(c)] and the S2 states [Figs. 7(f) and 7(g)] as a function of k and φ. The hexagonally shaped lines in panels Figs. 7(b) and 7(c) refer to the isoenergy lines at E_F, while the cicrles in panels Figs. 7(f) and 7(g) refer to energies 300 and 400 meV below E_F. Obviously, the in-plane spin component of the inner S1 state rotates clockwise, while the outer one rotates counterclockwise. Fortunately, for the spin-resolved MDC taken along the k_y direction through the $\overline{\mathrm{K}}_{\sqrt{3}}$ point [cf. Fig. 6(a)], the most intense peaks comprise spin signals only of the S1 state. For these states we calculated explicitly the spin orientations by Eqs. (2) and (3) (see Table I). As obvious for most spin components, both the magnitude and the direction are nicely reproduced by the Rashba model including higher-order corrections. On the other hand, the same calculation shows strong deviations from the experimental results for the $\overline{\Gamma\mathrm{M}}$ direction as shown in Table II. As obvious, the C_{3v} symmetry of our calculation can not explain the finite S_x and S_z components found in the experiment.

TABLE II. Peak parameters of the spin-polarized MDC along the $\overline{\Gamma \mathrm{M}}$ direction. The peaks **a–e** refer to the labels shown in Fig. 6(c). The spin components in the right part of the table are calculated by Eqs. (2) and (3) with the experimental values of S, showing deviations by symmetry breaking induced by both the imbalance of the rotational domains and the domain-wall formation.

			Spin components					
	Position	Polarization	Experiment			C_{3v} Rashba model		
Band, peak	k_x (Å^{-1})	S (%)	S_x (%)	S_y (%)	S_z (%)	S_x (%)	S_y (%)	S_z (%)
S1, **a**	0.35	99.9	−41.1	−49.0	−76.8	0	−99.9	0
S1, **b**	0.39	78.8	+37.0	+44.3	+53.6	0	+78.8	0
S1*/S2, **c**	0.50	44.4	−18.3	−14.8	−37.6	0	−44.4	0
S1, **d**	0.74	46.6	+25.2	−23.3	+31.5	0	−46.6	0
S1, **e**	0.77	96.4	−62.7	+47.2	−56.0	0	+96.4	0

We have mentioned above that the S2 state reveals a strong Zeeman-type splitting at the $\overline{\mathrm{K}}_{\sqrt{3}}$ points in agreement with DFT calculations [12,13]. In Figs. 7(f) and 7(g) we plotted the spin texture of the S2 state close to the $\overline{\mathrm{K}}_{\sqrt{3}}$ point. Compared to the S1 state, the S2 band is plotted with full S_y polarization along the k_x direction [in Figs. 7(f) and 7(g) we used renormalized coordinates with respect to the $\overline{\mathrm{K}}_{\sqrt{3}}$ point], as experimental values of S are missing at this point. Moreover, along the k_y direction (and equivalent directions) the spin is fully out-of-plane polarized. This peculiar spin texture is induced by an effective cycloidal magnetic field with C_{3v} symmetry around the $\overline{\mathrm{K}}_{\sqrt{3}}$ points, as depicted in Fig. 7(e), and takes the form

$$\mathbf{B}_{\mathrm{S}2}(\mathbf{k}') = B(k') \cdot \begin{pmatrix} +\cos(3\varphi)\sin\varphi \\ -\cos(3\varphi)\cos\varphi \\ -\sin(3\varphi) \end{pmatrix}, \tag{4}$$

giving rise to spin-polarization vectors

$$\mathbf{S}^{\pm}_{\mathrm{S}2}(\mathbf{k}) = \pm\frac{\hbar}{2} \cdot \frac{\mathbf{B}_{\mathrm{S}2}(\mathbf{k}')}{|\mathbf{B}_{\mathrm{S}2}(\mathbf{k}')|} \cdot S^{\pm}. \tag{5}$$

V. SUMMARY AND CONCLUSION

To summarize, our spin-resolved measurements are in excellent agreement with recent DFT calculations [12,13]. Albeit the unconventional Rashba splitting measured from states around the TRIMs is rather small ($\Delta k \approx 0.04$ Å^{-1}), the broken TRS at the $\overline{\mathrm{K}}_{\sqrt{3}}$ points reveals strong nonvortical spin textures with large energy splittings giving rise to strong spin polarization of the electron pockets around the $\overline{\mathrm{K}}_{\sqrt{3}}$ points. The detection of spin components, which are in the case of C_{3v} symmetry forbidden along the $\overline{\Gamma \mathrm{M}}$ direction, is caused by the imbalance of the rotational domains within the SIC phase. Aside from the Rashba splitting we found a new type of Zeeman-type spin splittings around the $\overline{\mathrm{K}}_{\sqrt{3}}$ points with a cycloidal spin texture. Moreover, we present a CEM, taken close to the Fermi energy E_{F}. Relying on recent calculations, we can accurately model the warping of the FS and and its spin texture in the framework of an anisotropic Rashba effect including higher-order terms in k.

The FS of high-coverage DS phases of Pb/Si(111) and β-Pb/Ge(111)-($\sqrt{3}\times\sqrt{3}$) show a similar flattening of the isoenergy lines giving rise to 2D Fermi nesting. The β-Pb/Ge(111)-($\sqrt{3}\times\sqrt{3}$) was assumed to undergo a CDW transition, which in fact was not observed for Pb/Si(111) down to 6 K [46]. For the SIC phase, the 2D nesting vectors are incommensurate with the atomic structure. Obviously, this mechanism keeps the system immune against CDW formation and enables a superconducting behavior at low temperatures.

ACKNOWLEDGMENTS

We thank P. Kratzer from the Duisburg-Essen University for stimulating discussions. This work is financially supported by the Deutsche Forschungsgemeinschaft (DFG) within Grant No. FOR1700.

---

[1] J. M. Carpinelli, H. H. Weitering, W. W. Plummer, and R. Stumpf, Nature (London) **381**, 398 (1996).

[2] A. Mascaraque, J. Avila, E. G. Michel, and M. C. Asensio, Phys. Rev. B **57**, 14758 (1998).

[3] T. Hirahara, T. Komorida, Y. Gu, F. Nakamura, H. Idzuchi, H. Morikawa, and S. Hasegawa, Phys. Rev. B **80**, 235419 (2009).

[4] T. Zhang *et al.*, Nat. Phys. **6**, 104 (2010).

[5] M. Yamada, T. Hirahara, and S. Hasegawa, Phys. Rev. Lett. **110**, 237001 (2013).

[6] C. Brun *et al.*, Nat. Phys. **10**, 444 (2014).

[7] D. Roditchev, C. Brun, L. Serrier-Garcia, J. C. Cuevas, V. H. L. Bessa, M. V. Milošević, F. Debontridder, V. Stolyarov, and T. Cren, Nat. Phys. **11**, 332 (2015).

[8] C. Brun, T. Cren, and D. Roditchev, Supercond. Sci. Technol. **30**, 013003 (2017).

[9] M. Hupalo, J. Schmalian, and M. C. Tringides, Phys. Rev. Lett. **90**, 216106 (2003).

[10] K. Budde, E. Abram, V. Yeh, and M. C. Tringides, Phys. Rev. B **61**, R10602 (2000).

[11] M. C. Tringides, M. Hupalo, K. L. Man, M. M. T. Loy, and M. S. Altman, in *Wetting Layer Super-Diffusive Motion*

and QSE Growth in Pb/Si in Nanophenomena at Surfaces: Exotic Condensed Matter Properties, edited by M. Michailov (Springer, New York, 2011).

[12] S. Sakong, P. Kratzer, S. Wall, A. Kalus, and M. Horn-von Hoegen, Phys. Rev. B **88**, 115419 (2013).

[13] X.-Y. Ren, H.-J. Kim, S. Yi, Y. Jia, and J.-H. Cho, Phys. Rev. B **94**, 075436 (2016).

[14] J. H. Dil, F. Meier, J. Lobo-Checa, L. Patthey, G. Bihlmayer, and J. Osterwalder, Phys. Rev. Lett. **101**, 266802 (2008).

[15] B. Slomski, G. Landolt, G. Bihlmayer, J. Osterwalder, and J. H. Dil, Sci. Rep. **3**, 1963 (2013).

[16] G. Li, P. Höpfner, J. Schäfer, C. Blumenstein, S. Meyer, A. Bostwick, E. Rotenberg, R. Claessen, and W. Hanke, Nat. Commun. **4**, 1620 (2013).

[17] C. Brand, H. Pfnür, G. Landolt, S. Muff, J. H. Dil, T. Das, and C. Tegenkamp, Nat. Commun. **6**, 8118 (2015).

[18] F. Meier, J. H. Dil, and J. Osterwalder, New J. Phys. **11**, 125008 (2009).

[19] Y. A. Bychkov and É. I. Rashba, Pis'ma Zh. Eksp. Teor. Fiz. **39**, 66 (1984) [JETP Lett. **39**, 78 (1984)].

[20] Y. A. Bychkov and É. I. Rashba, J. Phys. C: Solid State Phys. **17**, 6039 (1984).

[21] J. H. Dil, J. Phys.: Condens. Matter **21**, 403001 (2009).

[22] K. Sakamoto, H. Kakuta, K. Sugawara, K. Miyamoto, A. Kimura, T. Kuzumaki, N. Ueno, E. Annese, J. Fujii, A. Kodama *et al.*, Phys. Rev. Lett. **103**, 156801 (2009).

[23] P. Höpfner, J. Schafer, A. Fleszar, J. H. Dil, B. Slomski, F. Meier, C. Loho, C. Blumenstein, L. Patthey, W. Hanke, and R. Claessen, Phys. Rev. Lett. **108**, 186801 (2012).

[24] K. Sakamoto *et al.*, Nat. Commun. **4**, 2073 (2013).

[25] P. Eickholt, P. Krüger, S. D. Stolwijk, A. B. Schmidt, and M. Donath, Phys. Rev. B **93**, 085412 (2016).

[26] K. Sakamoto, T. Oda, A. Kimura, Y. Takeichi, J. Fujii, R. I. G. Uhrberg, M. Donath, and H. W. Yeom, J. Electron Spectrosc. Relat. Phenom. **201**, 88 (2015).

[27] K. Nakajin and S. Murakami, Phys. Rev. B **91**, 245428 (2015).

[28] C.-S. Tang, S.-T. Tseng, V. Gudmundsson, and S.-J. Cheng, J. Phys.: Condens. Matter **27**, 085801 (2015).

[29] L. Fu, Phys. Rev. Lett. **103**, 266801 (2009).

[30] K. Kuroda, M. Arita, K. Miyamoto, M. Ye, J. Jiang, A. Kimura, E. E. Krasovskii, E. V. Chulkov, H. Iwasawa, T. Okuda *et al.*, Phys. Rev. Lett. **105**, 076802 (2010).

[31] P. Höpfner, J. Schafer, A. Fleszar, S. Meyer, C. Blumenstein, T. Schramm, M. Hessmann, X. Cui, L. Patthey, W. Hanke, and R. Claessen, Phys. Rev. B **83**, 235435 (2011).

[32] K. Yaji, Y. Ohtsubo, S. Hatta, H. Okuyama, K. Miyamoto, T. Okuda, A. Kimura, H. Namatame, M. Taniguchi, and T. Aruga, Nat. Commun. **1**, 17 (2010).

[33] W. H. Choi, H. Koh, E. Rotenberg, and H. W. Yeom, Phys. Rev. B **75**, 075329 (2007).

[34] V. Yeh, M. Yakes, M. Hupalo, and M. C. Tringides, Surf. Sci. **562**, L238 (2004).

[35] M. Hoesch, T. Greber, V. N. Petrov, M. Muntwiler, M. Hengsberger, W. Auwärter, and J. Osterwalder, J. Electron Spectrosc. Relat. Phenom. **124**, 263 (2002).

[36] J. Noffsinger and M. L. Cohen, Solid State Commun. **151**, 421 (2011).

[37] T.-L. Chan, C. Z. Wang, M. Hupalo, M. C. Tringides, Z.-Y. Lu, and K. M. Ho, Phys. Rev. B **68**, 045410 (2003).

[38] A. Baumann, E. Speiser, S. Chandola, J. Räthel, P. Kratzer, S. Sakong, C. Tegenkamp, and N. Esser (unpublished).

[39] L. Seehofer, G. Falkenberg, D. Daboul, and R. L. Johnson, Phys. Rev. B **51**, 13503 (1995).

[40] S. Stepanovsky, M. Yakes, V. Yeh, M. Hupalo, and M. C. Tringides, Surf. Sci. **600**, 1417 (2006).

[41] J. M. Carpinelli, H. H. Weitering, M. Bartkowiak, R. Stumpf, and E. W. Plummer, Phys. Rev. Lett. **79**, 2859 (1997).

[42] H. Daimon, S. Imada, H. Nishimoto, and S. Suga, J. Electron Spectrosc. Relat. Phenom. **76**, 487 (1995).

[43] Sz. Vajna, E. Simon, A. Szilva, K. Palotas, B. Ujfalussy, and L. Szunyogh, Phys. Rev. B **85**, 075404 (2012).

[44] We calculated the eigenenergies in Eq. (1) with change of cos ↔ sin in the Rashba term for symmetry reasons including TRS, in contrast to Vajna [43].

[45] K. Yaji, S. Hatta, T. Aruga, and H. Okuyama, Phys. Rev. B **86**, 235317 (2012).

[46] H. Morikawa, I. Matsuda, and S. Hasegawa, Phys. Rev. B **77**, 193310 (2008).